Indentation of living cells by AFM tips may not be what we thought!

Ophélie Thomas- -Chemin, Childérick Séverac, Emmanuelle Trévisiol, Etienne Dague

Indentation of living cells by AFM tips may not be not what we thought!

Ophélie Thomas - - Chemin,[1] Childérick Séverac,[2] Emmanuelle Trevisiol[3] and Etienne Dague[1,*]

[1]LAAS-CNRS, Université de Toulouse, CNRS, Toulouse France

[2]RESTORE Research Center, Université de Toulouse, INSERM, CNRS, EFS, ENVT, Université P. Sabatier, Toulouse, France

[3]TBI, Université de Toulouse, CNRS, INRAE, INSA, Toulouse, France

[*]edague@laas.fr

Abstract

The models used to calculate Young's moduli from atomic force microscopy (AFM) force curves consider the shape of the indentation. It is then assumed that the geometry of the indentation is identical to the geometry of the indenter, which has been verified for hard materials (E > 1 MPa). Based on this assumption, the force curves calculated by these models, for the same object with a given Young's modulus, are different if the indenter geometry is different. On the contrary, we observe experimentally that the force curves recorded on soft living cells, with pyramidal, spherical, or tipless indenters, are almost similar. This indicates that this basic assumption on the indentation geometry does not work for soft materials (E of the order of 5 kPa or less). This means that, in this case, the shape of the indentation is therefore different from the shape of the indenter. Indentation of living cells by AFM is not what we thought!

1. Introduction

Nanomechanical measurements on living cells by AFM have now been described for about 30 years (Radmacher et al., 1996). The principle is to indent into the soft material that is a cell with an indenter mounted on a cantilever presenting a spring constant close to that of the cell. The geometry of the indenter is usually a pyramid (Sirghi et al., 2008), or a sphere (Hiratsuka et al., 2009) and can occasionally be a bare cantilever (Abraham et al., 2021). Depending on the context of the studies and to calculate the biomechanical properties of a sample, authors deduce and calculate either the cell stiffness (also called the cell spring constant (Gibbs et al., 2021)) or the Young's modulus of the cells from the indentation force curves; this is usually done using the Hertz model adapted to the indenter geometry (Dokukin et al., 2013; Gibbs et al., 2021).

Whatever the model used to fit the force *versus* indentation curves, these calculations of Young's modulus have always been very dependent on several factors: first, the tip calibration is a key problem

and attracted the attention of researchers (Hutter and Bechhoefer, 1993; Sader et al., 1999; te Riet et al., 2011; Schillers et al., 2017). Secondly the result of the fit is highly dependent on the contact point position, which is not so easy to identify on force curves recorded on living cells (Kontomaris et al., 2022; Lin et al., 2007; Roduit et al., 2012, 2009). Third, the portion of the indentation curve that is fitted can completely change the result of Young's modulus (Lee et al., 2018; Pogoda et al., 2012). Finally, the calculation requires to use the Poisson's ratio, which allows to characterize the contraction of the material perpendicular to the direction of the applied force. This ratio is globally sparsely measured (Hurley and Turner, 2007; Song et al., 2018), but is usually settled at 0.45 or 0.5 in water, which definitively prevent to provide an absolute value of cells Young's modulus. These points are good candidates to explain that one can find in the literature very different Young's modulus values for the same biological object and that only relative comparisons are valid. Table 1 is gathering a few examples of Young's modulus values that can be found in the literature: bladder carcinoma cell lines Hu609 and HCV29 range from 3.29 to 9.7 kPa (Lekka et al., 2012, 1999) and 3.19 to 33 kPa (Lekka et al., 2012; Ramos et al., 2014), respectively; those of prostate cancer LNCaP and PC3 ranged from 0.287 to 0.46 kPa (Faria et al., 2008; Lekka et al., 2012) and 1.401 to 2.53 kPa (Deliorman et al., 2020; Faria et al., 2008), respectively; and those of the breast MCF7, MDA-MB-231, and MCF10A ranged from 0.4 to 87.3 kPa (Coceano et al., 2015; Fischer et al., 2020), 0.34 to 55.6 kPa (Coceano et al., 2015; Jonas et al., 2011), and 0.48 to 1.11 kPa (Jonas et al., 2011 ; Nikkhah et al., 2011), respectively.

Cell lines	**Young's moduli (kPa)**	**Tips shapes**	**Cantilever's spring constant (N/m)**	**Length of indentation segment (nm)**	**Speed (µm/s)**	**Poisson's ratio**	**References**
Hu609	9.7 ± 3.6	Pyramid (20-30 nm-diameter)	0.1, 0.03 and 0.05	2 000	0.19	0.5	(Lekka et al., 1999) [1]
	3.29 ± 0.35	Pyramid (35 °-open angle)		500	5	0.5	(Lekka et al., 2012) [2]
HCV29	7.5 ± 3.6	Pyramid (20-30 nm-diameter)	0.1, 0.03 and 0.05	2 000	0.19	0.5	(Lekka et al., 1999) [3]
	3.19 ± 0.27	Pyramid (35 °-open angle)		500	5	0.5	(Lekka et al., 2012) [4]
	16.0 ± 0.9 / 33.0 ± 2.0	V-shaped/Pyramid (MLCT-C) (20 °-half angle)	0.01	300	5	0.5	(Ramos et al., 2014) [5]
T24	0.77 ± 0.25	Pyramid (35 °-open angle)		500	5	0.5	(Lekka et al., 2012) [6]
Hu456	0.80 ± 0.23	Pyramid (35 °-open angle)		500	5	0.5	(Lekka et al., 2012) [7]
BC3726	0.17 ± 0.08	Pyramid (35 °-open angle)		500	5	0.5	(Lekka et al., 2012) [8]
LNCaP	0.287 ± 0.052	Pyramid	0.06	3 000	5.7		(Faria et al., 2008) [9]

	0.46 ± 0.17	Pyramid (35 °-open angle)		400	5	0.5	(Lekka et al., 2012) [10]
PC3	1.401 ± 0.162	Pyramid	0.06	3 000	5.7		(Faria et al., 2008) [11]
	1.97 ± 0.41	Pyramid (35 °-open angle)		400	5	0.5	(Lekka et al., 2012) [12]
	2.53 ± 0.13	Colloid (6 µm-diameter)	0.08	400	4	0.5	(Deliorman et al., 2020) [13]
RWPE-1	6.055 ± 0.49	Colloid (500 nm-diameter)		500		0.5	(Parihar et al., 2022) [14]
	6.2 ± 2.4	Colloid (1 µm-diameter)	0.8			0.5	(Pogoda et al., 2012) [15]
MCF7	0.40 ± 0.12 (nucleus)	Colloid (6 µm-diameter)					(Fischer et al., 2020) [16]
	1.24 ± 0.46	Pyramid (35 °-open angle)		400	5	0.5	(Lekka et al., 2012) [17]
	87.3 ± 47.8 (nucleus)	Pyramid (18 °-half angle)	0.35	200		0.4	(Coceano et al., 2015) [18]
	0.43 ± 0.031	Tipless	0.15				(Jonas et al., 2011)
	1.04	Pyramid (17.5 °-half angle)	0.03	500	4	0.5	(Omidvar et al., 2014) [19]
	0.40 ± 0.30	Colloid (5 µm-diameter)	0.069			0.5	(Dokukin et al., 2013) [20]
	5.5 ± 0.8 (nucleus)	Pyramid		1 000	2		(Wu et al., 2018) [21]
	0.81 ± 0.06	Colloid (5 µm-diameter)		300	6		(Wu et al., 2018) [21]
MDA-MB-231	55.6 ± 20.1 (nucleus)	Pyramid (18 °-half angle)	0.35	200		0.4	(Coceano et al., 2015) [22]
	0.5 ± 0.35 (in RPMI + 10 % FBS)	Colloid (10 µm-diameter)	0.02	200	0.5	0.5	(Nikkhah et al., 2011) [23]
	0.341 ± 0.041	Tipless	0.15				(Jonas et al., 2011)
	0.62	Pyramid (17.5 °-half angle)	0.03	500	4	0.5	(Omidvar et al., 2014) [24]
	0.74 ± 0.29	Sphero-conical (22.5 °- half angle)	0.15	250 – 2 500		0.45	(Staunton et al., 2016)
	0,51 ± 0,35	Colloid (10 µm-diameter)	0.02		0.5	0.5	(Strobl et al., 2010) [25]
	0.1577 ± 0.07855 (nucleus)	Colloid (6 µm-diameter)	0.02			0.5	(Fischer et al., 2020) [26]
MCF10A	1.11 ± 0.85 (in RPMI + 10 % FBS)	Colloid (10 µm-diameter)	0.02	182	0.5	0.5	(Nikkhah et al., 2011) [27]
	0.48 ± 0.069	Tipless	0.15				(Jonas et al., 2011)

	0.59 ± 0.54 (nucleus)	Colloid (6 µm-diameter)					(Fischer et al., 2020) [28]
T47D	0.94	Pyramid (17.5 °-half angle)	0.03	500	4	0.5	(Omidvar et al., 2014) [29]
HMEC	1.01 ± 0.52	Colloid (5.3 µm-diameter)	0.035	600 – 1 000	4	0.5	(Lee et al., 2021) [30]
NHLF	16.67 ± 0.75	Pyramid		400			(Orzechowska et al., 2022) [31]
IPF	19.70 ± 0.81	Pyramid		400			(Orzechowska et al., 2022) [32]
IOSE	2.472 ± 2.048	Colloid (4.7 µm-diameter)	0.03	1 000			(Xu et al., 2012) [33]
OVCAR4	1.120 ± 0.865	Colloid (4.7 µm-diameter)	0.03	1 000			(Xu et al., 2012) [34]
OVCAR5	0.64 ± 0.03	Pyramid	0.02				(Sharma et al., 2012) [35]
SKOV3	0.41 ± 0.04	Pyramid	0.02				(Sharma et al., 2012) [36]
HEY	0.884 ± 0.529	Colloid (4.7 µm-diameter)	0.03	1 000			(Xu et al., 2012) [37]
WM115	2.17 ± 0.22	Pyramid (35 °-open angle)		500	5	0.5	(Lekka et al., 2012) [38]
WM266-4	1.48 ± 0.28	Pyramid (35 °-open angle)		500	5	0.5	(Lekka et al., 2012) [39]
BALB 3T3	1.01 ± 0.40	Colloid (1.5 – 4 µm)	0.02 – 0.06			0.5	(Park et al., 2005) [40]
SV-T2	0.48 ± 0.51	Colloid (1.5 – 4 µm)	0.02 – 0.06			0.5	(Park et al., 2005) [41]

Table 1 – Different Young's moduli found on cell lines depending on the type of tip, spring constant of the cantilever, length of the indentation segment and Poisson's ratio. These articles have been cited because they specify the different parameters used during AFM measurements.

Moreover, the geometry of the indentation and thus of the indenter needs to be modeled accordingly. Nevertheless, in the case of very soft living cells, the assumption that indenter and indentation geometry are comparable is not so obvious (Harris, A. & Charras, G., 2011). From Table 1, plotting the Young's moduli as a function of the indenter shape (Fig. 1A-B), of the spring constant of the cantilever (Fig. 1C-D) or of the indentation depth (Fig. 1E-F), a weak correlation can be found. Pyramid tips are the only ones to provide Young's moduli higher than 10 kPa and up to 87.3 kPa. Fig. 1C-D shows the weak link between the Young's modulus and the spring constant of the cantilever. The higher the spring constant, the higher the Young's modulus, this is not so surprising because indentation in a rigid material requires a stiff cantilever. In Fig. 1E, one can also see a correlation between the Young's modulus and the indentation segment, this is also not surprising because fitting a short indentation segment results in smaller Young's modulus than fitting a large indentation segment. Fortunately, these results show weak correlations, because the cell lines used for this analysis are different by

nature. A strong correlation would have pointed out an important artefact in Young's modulus calculation. The conclusion of this analysis is that relative comparisons are probably true but that artefact due to indenter shape, spring constant determination or indentation depth, are also playing a role on the absolute values calculations.

In this paper, we challenge this discrepancy between low Young's moduli when indenter and/or model are spherical and higher Young's moduli when the cell is probed with a sharper indenter and calculated with a model that considers the sharpness of the indenter. We made the disruptive hypothesis that the indenter geometry may not reflect the indentation geometry in the case of especially soft materials such as cells. To test this hypothesis, we probed living mammalian cells (PC3-GFP) with indenters of different geometries and calculated the Young's moduli with the corresponding formula (pyramid is presented in red, colloid in blue and tipless in green). We then plotted the raw force curves obtained with the different indenters, together with the force curves expected from the models.

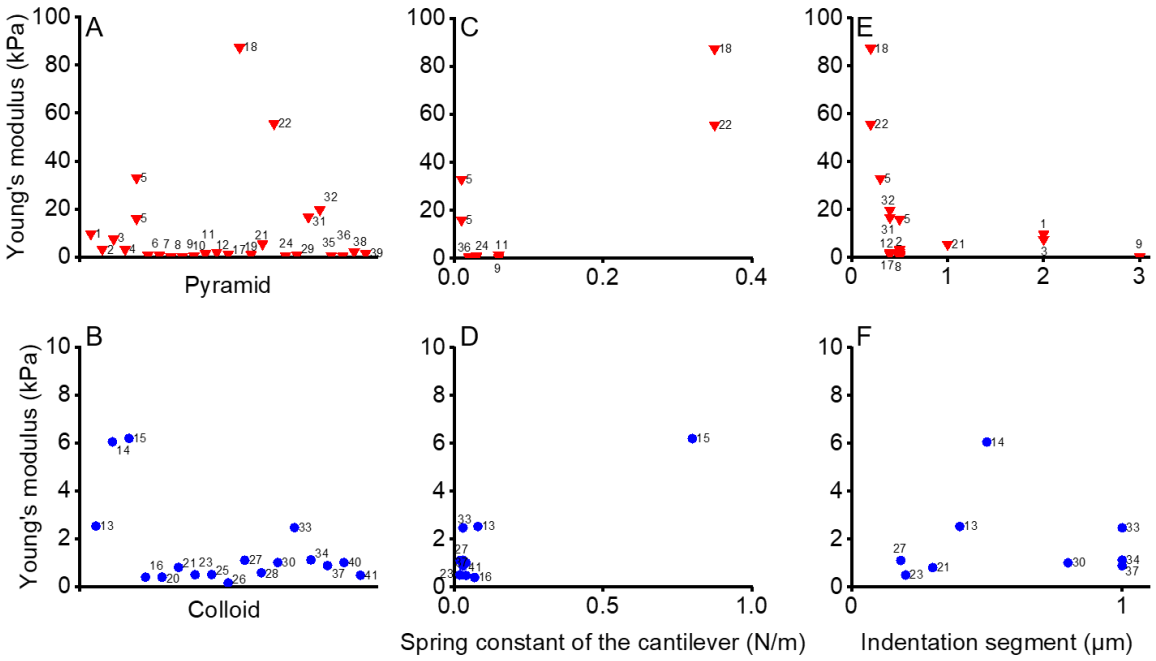

Figure 1 – Young's modulus values as a function of cantilever properties and indentation segment. (**A-B**) Reported Young's modulus values from Table 1 references as a function of the indenter geometry for a pyramidal (**A**) and a colloidal (**B**) tip. (**C-D**) Young's modulus values reported from the references in Table 1 as a function of the cantilever spring constant for a pyramidal (**C**) and a colloidal (**D**) tip. (**E-F**) Young's modulus values reported from the references in Table 1 as a function of indentation segment length for a pyramidal (**E**) and a colloidal (**F**) tip. Numbers next to the points correspond to the bibliographic references presented in Table 1.

2. Material and methods

2.1. Cell culture

The PC3-GFP cell line was cultured in RPMI medium, containing L-glutamine, HEPES buffer and phenol red (Gibco™, Thermo Fisher Scientific Inc.) with 10% foetal bovine serum (FBS, Gibco™, Thermo Fisher

Scientific Inc.), 1% penicillin-streptomycin (Gibco™, Thermo Fisher Scientific Inc.) and 1% geneticin (G418, Gibco™, Thermo Fisher Scientific Inc.) in a 37 °C incubator and 5% CO_2. The cells were then seeded on 20 mm side glass coverslips at a concentration of 30 000 cells per cm² and placed in 40 mm diameter Petri dishes overnight.

2.2. Production of cell arrays

We use cell arrays to obtain spatially reproducible measurements and to reduce dispersion within our populations, whatever the indenters used. In this way, we can map a cell in a similar way with pyramidal, colloidal or tipless indenters. The production of cell arrays follows a two-step process: i) microcontact printing (µCP) of fibronectin patterns using the InnoStamp 40™ device (Lagraulet et al., 2015); ii) cell seeding.

2.2.1 Microcontact printing

Micropatterned PDMS stamps (40 x 40 µm² squares), fabricated according to Fredonnet et al., 2013, were deposited at the loading zone of the InnoStamp 40™. The glass slide was cleaned 10 seconds with acetone, 10 seconds with deionized water and 10 seconds with isopropanol before undergoing an oxygen plasma treatment (Diener Pico, 50 W, 0.3 mbar, 1 min 30). It was then placed on the deposition area of the InnoStamp 40™. 71 µL of bovine plasma fibronectin (Sigma Aldrich, Merck KGaA.) at a concentration of 100 µg/mL (in 1 X PBS, pH 7.4, NaCl: 137 mM; KCl: 2.7 mM; Na_2HPO_4: 10 mM; KH_2PO_4: 1.8 mM) were deposited on a glass slide at the inking zone of the Innostamp 40™. The automated µCP protocol was then initiated and consisted of inking the surface of the PDMS stamps with fibronectin, followed by drying and finally µCP of the fibronectin onto the glass slide. The functionalized coverslip was removed from the InnoStamp 40™ and placed in a 40 mm diameter Petri dish. 200 µL of PLL-g-PEG (PLL (20)-g [3.5]-PEG (2), SuSoS AG.) at a concentration of 100 µg/mL (in 1X PBS, pH 7.4) was poured onto the glass coverslip and after a 30 min incubation, the coverslip was rinsed 3 times with 1X PBS, pH 7.4.

2.2.2. Cell seeding

1 mL of PC3-GFP cells, at a concentration of 72 000 cells/mL, were seeded in RPMI medium, containing L-glutamine, HEPES buffer and phenol red (Gibco™, Thermo Fisher Scientific Inc.) with 10% foetal bovine serum (SVF, Gibco™, Thermo Fisher Scientific Inc.), 1 % penicillin-streptomycin (Gibco™, Thermo Fisher Scientific Inc.), and 1 % geneticin (G418, Gibco™, Thermo Fisher Scientific Inc.) on glass coverslips placed in 40-mm-diameter Petri dishes supplemented with 2 mL of culture medium in an incubator at 37 °C and 5 % CO_2. At 1 hour after seeding, the culture medium was changed to remove nonadherent cells. Then, the cells were incubated overnight before AFM measurements.

2.3. AFM measurements. Calibration of the cantilevers: sensitivity and spring constant

Force spectroscopy AFM experiments were performed on an AFM NanoWizard® 3 device (JPK Instruments, Bruker Nano GmbH.) in contact mode, force mapping. Three types of cantilever geometries were used. These are MLCT-BIO-DC pyramidal tips in triangular shape (20 nm radius; 17.5 ° half-aperture angle), colloidal tips from NP-O10 tipless cantilevers with 5.0 µm in diameter silica beads (from Bang Laboratories) (protocol described in (Dramé et al., 2020) and NP-O10 tipless cantilevers all from Bruker. Before each experiment, the sensitivity of the AFM photodiode-cantilever system was measured by calculating the slope of the laser *versus* piezo position curve. In this study, pyramidal tip with a sensitivity of 38.22 nm/V to 50.25 nm/V were used; colloidal shaped cantilevers sensitivity ranged from 33.49 nm/V to 35.31 nm/V and tipless cantilevers sensitivity was 47.14 nm/V. The spring constant was then calibrated using the thermal fluctuation of the cantilever at 37 °C (Hutter and Bechhoefer, 1993). In this study, the MLCT-BIO-DC pyramidal cantilevers had spring constants of 0.011 N/m, the colloidal cantilevers between 0.018 N/m and 0.056 N/m and the tipless cantilevers of 0.021 N/m. The force mapping measurements and images were performed in the buffered culture medium at 37 °C, with a relative setpoint of 3 nN, a Z-length of 5 µm, an extend velocity of 50 µm/s and in 32 x 32 pixels on areas of 10 x 10 µm².

2.4. Comparison of measured and theoretical Young's modulus values

One of the issues of AFM experiments is to be able to calculate a Young's modulus from a measured force curve. For this, mathematical models accounting for the force applied on an object have been developed. They depend on the indentation depth of the indenter and its geometry: for a pyramidal indenter, the Sneddon model:

$$F_{Cone} = \frac{3}{4}\frac{(E)}{1-\nu^2}\ tan\,\theta\ \delta^2 \ (Eq.\ 1)$$

where *F* is the force applied to the sample, *E* the Young's modulus, *v* is the Poisson's ratio, which is considered equal to 0.5 for soft biological samples, *δ* the indentation and θ the half-open angle of the pyramid, i.e. 17.5 ° for the MLCTs cantilevers.

for a colloidal indenter, the Hertz model for a sphere:

$$F_{Sphere} = \frac{4}{3}\frac{(E)}{1-\nu^2}\ \sqrt{R}\ \delta^{3/2} \ (Eq.\ 2)$$

where *F* is the force applied to the sample, *E* the Young's modulus, *v* is the Poisson's ratio, which is considered equal to 0.5 for soft biological samples, *δ* the indentation and *R* the radius of the sphere, i.e. 2.52 µm for Microspheres beads.

and for a tipless indenter, the Hertz model for a cylinder:

$$F_{Cylinder} = \frac{2(E)a}{1-v^2}\ \delta \ (Eq.\ 3)$$

where *F* is the force applied to the sample, *E* the Young's modulus, *v* is the Poisson's ratio, which is considered equal to 0.5 for soft biological samples, *δ* the indentation and *a* the radius of the cylinder, i.e. 25 µm for the NP-Os.

Respective Young's moduli were calculated using JPK Data Processing software (v6.1.183) using these formulas.

2.5. SEM imaging

SEM images were taken on a Hitachi S4800 SEM. AFM tips were loaded onto a pre-tilted holder. All images were taken at 1 kV.

3. Results

Force *versus* distance curves were recorded on living PC3 cells using pyramidal indenters (MLCT-BIO-DC from Bruker), spherical indenters (NP-O10 modified with silica beads from Bang Laboratories) and tipless cantilevers (NP-O10 from Bruker) (Fig. 2A-C). We first report the Young's modulus that we calculated, with different AFM tip geometries (pyramidal, colloidal and tipless) (Fig. 2) and related models.

Ten cells were measured with each indenter and 1 024 force curves were recorded on a 10 x 10 µm^2 area on each cell. Fig. 2D-F present the Young's modulus repartition calculated respectively with a pyramidal (Eq. 1), a colloidal (Eq. 2) and a tipless (Eq. 3) cantilever. We decided to fit a fixed portion of 0.5 µm of the force *versus* indentation curve and the cantilever spring constant ranged from 0.011 to 0.056 N/m. Fig. 2G-I show the Young's modulus maps recorded on 10 x 10 µm² demonstrating the homogeneity at the scale of the cell surface. The calculated Young's modulus values are 1.7 ± 1.1 for a pyramidal tip, 0.2 ± 0.2 for a colloidal tip and 0.004 ± 0.002 kPa for a tipless cantilever. Young's modulus values of the cells are 9 times higher with the pyramidal tip compared to the colloidal one, 50 times higher with the colloidal tip compared to the bare tip and even 425 times higher with the pyramidal tip compared to the tipless indenter. We would have expected almost the same values since they are measurements of the same biological objects; this means that two or all of the values are inaccurate and we need to go further in the interpretation.

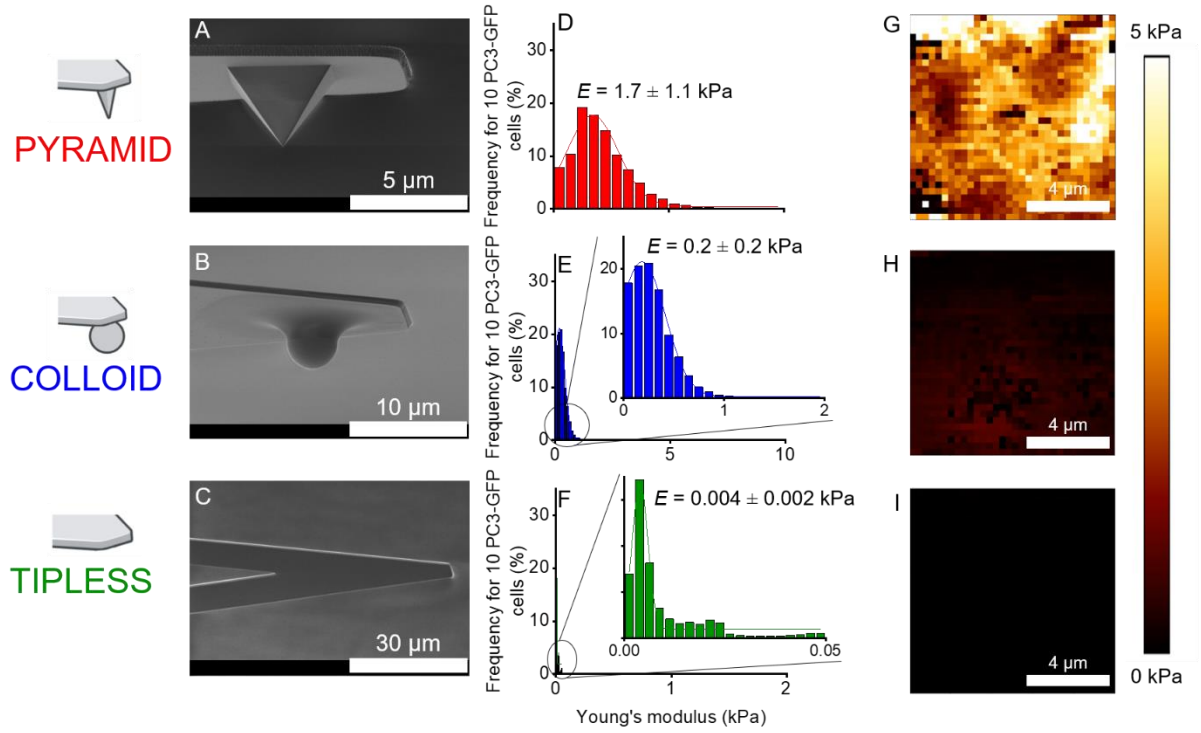

Figure 2 – Comparison of Young's modulus values obtained from pyramidal, colloidal or tipless cantilever experiment calculated with the related models. (**A-C**) SEM images of a pyramidal probe (**A**), a colloidal probe (**B**) and a bare probe (**C**). (**D-F**) Distributions of the Young's modulus calculated on 10 PC3-GFP cells arranged on 40 µm-square patterns measured with a pyramidal probe (**D**), a colloidal probe (**E**) and no tip (**F**). The fits are made on 500 nm of indentation. (**G-I**) Young's modulus maps calculated with a pyramidal probe (**G**), a colloidal probe (**H**) and a bare probe (**I**) of the cell surface. n_{FCs} = 10 240.

To better understand this phenomenon, we reversed the problem and plotted the theoretical force *versus* indentation curves calculated with Eqs. 1, 2 and 3 (Fig. 3A), for theoretical materials of 0.5, 5 and 50 kPa. As expected pyramidal indenters are going deeper in the material than colloidal or tipless probes for the same applied force. For example, the theoretical force indentation curve calculated for a pyramid indenting a theoretical material of 5 kPa is comparable with a theoretical indentation curve calculated for a colloidal tip indenting a theoretical material of 0.5 kPa. This means that for an experimental force curve, the Young's modulus is 10 times higher if it is calculated with the pyramidal model instead of the colloidal model. This is close to what we observe (Young's calculated with a pyramid is 9 times higher than Young's modulus calculated with a colloid). Furthermore, the experimental indentation curves obtained with the different indenters on the same graph (Fig. 3B) almost overlap. This is unexpected and it means that the indenter geometry does not change the experimental result. This can be due to at least 2 reasons: i) Local measurements are different from global measurements. They are much more heterogeneous. However, the measurements taken with the large indenters are averages of the local properties and so the average of the local measurements should not differ from the global measurements, but they are as this is illustrated by the Young's modulus maps presented Fig. 2G-I. On the other hand, it is normal for the standard deviations to be

higher. ii) what is actually indenting is not what we think… and the indenter geometry has little to do with the geometry of the indentation and therefore the application of models considering the geometry of the indentation equivalent to the indenter geometry create a misinterpretation.

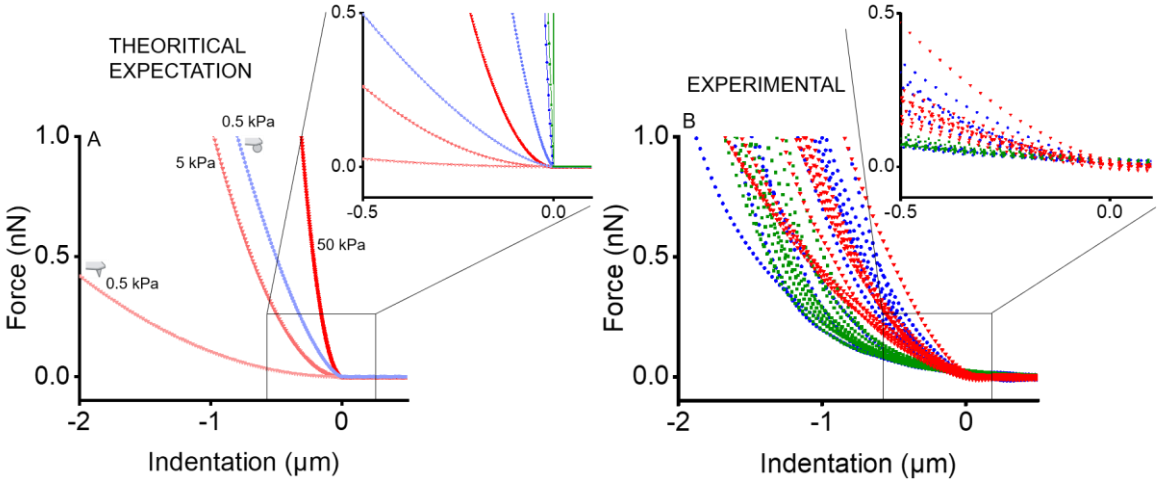

Figure 3 – Comparison of force-indentation curves as a function of AFM tip geometry. (**A**) Theoretical representations of the force-indentation curves calculated with the cone ($F_{Cone} = \frac{3}{4}\frac{(E)}{1-\nu^2}\ \tan\theta\ \delta^2$ -pyramid- red), sphere ($F_{Sphere} = \frac{4}{3}\frac{(E)}{1-\nu^2}\sqrt{R}\ \delta^{\frac{3}{2}}$ -colloid- blue) or without tip ($F_{Cylinder} = \frac{2(E)a}{1-\nu^2}\ \delta$, where a = 25 µm, green) models when indenting theoretical samples displaying Young's modulus of 0.5 (lightest colour), 5 or 50 kPa (darkest colour). (**B**) Experimental force-indentation recorded on living cells with a pyramidal (red), colloidal (blue), and no tip (green). For each condition, n_{cells} = 10 and n_{FCs} = 10.

In theory (Fig. 3A), to have the same indentation depth of 0.5 µm, the force applied by the colloid should be 20 times higher than that of the pyramid and 600 times lower than that of the tipless cantilever (Fig. 3A). Experimentally (Fig. 3B), it is not what we measure (0.08 nN to indent 0.5 µm with a tipless cantilever and in between 0.1 and 0.5 nN to indent 0.5 µm with a colloid or a pyramid).

Discussion

Numerous studies have attempted to model and simulate the indentation of an AFM tip in a cell, considering the geometry of the indenter (conical or spherical) and the indentation are similar (Fig. 4A,C) (Esteki et al., 2020; Sen et al., 2005). However, this assumption is usually not experimentally validated. Conversely, some rare publications tackled this issue and relied on images taken with a side-view system and a confocal microscope to visualize the true indentation geometry (Fig. 4B,D,E) (Harris, A. & Charras, G., 2011; Moeendarbary et al., 2013). Harris *et* Charras found that the contact area between the pyramidal tips and cells does not look like a cone, for applied forces higher than 0.2 nN, which agrees with our observations. The authors also find that pyramidal tips give larger elasticity values than spherical tips. This can be explained by the larger contact area considered by the spherical tip model compared with the pyramidal tip model. Finally, they were able to show that the

experimentally measured contact area for spherical tips well corresponds to the predicted values, whereas for pyramidal tips, the contact area is largely underestimated leading to a 2-fold overestimation of the elasticity.

The current consensus in the field is that spherical indenters average measurements because they probe a larger area and that more localized results can be obtained using a sharper indenter such as a pyramid (Rico et al., 2005; Zemła et al., 2020; Kulkarni et al., 2023). In these articles, the authors attribute the differences in calculated Young's moduli to the fact that the mechanical properties measured locally or globally are different. Without the force curves obtained with the different indenter geometries and at the same deflection height scale, it is impossible to verify whether the differences in calculated Young's moduli are also due to the application of different models to an identical indentation geometry. However, if the result obtained with a spherical indenter is an average, it should not be an order of magnitude larger or smaller than the result obtained with a sharper indenter. However, this is what is found in our experiments. One of the hypotheses explaining this result could be the high tip velocity that we used (50 µm/s). Force spectroscopy at 50 µm/s is rare, as it can be seen in Table 1, most of the measurements in the literature were carried out between 0.19 and 5.7 µm/s. To address this issue, we performed micro-rheology measurement to ensure that we were probing the cells in the elastic regime. The results are presented in the Supp. Fig. S3 and demonstrate that the shear storage (G') is 2 times higher than the shear loss (G'') at a tip velocity of 50 µm/s. Even at 100 and 200 µm/s (respectively 10 and 20 Hz) G'' is still smaller than G' which means that the visoelastic regime has still not been reached. This shows that at the tip velocity of 50µm/s, cells behave elastically. Furthermore, in Rico et al., 2005, the force curves recorded on cells with a pyramidal indenter and a colloidal indenter are overlapped, which we also present. This can be explained by the fact that the indentation geometry is different from the indenter geometry, especially as the cantilevers are approached from their samples at an angle of 10 °, which changes the geometry of the indentation for some pyramidal and tipless cantilevers. Models considering indenter geometry here provided false absolute Young's modulus values.

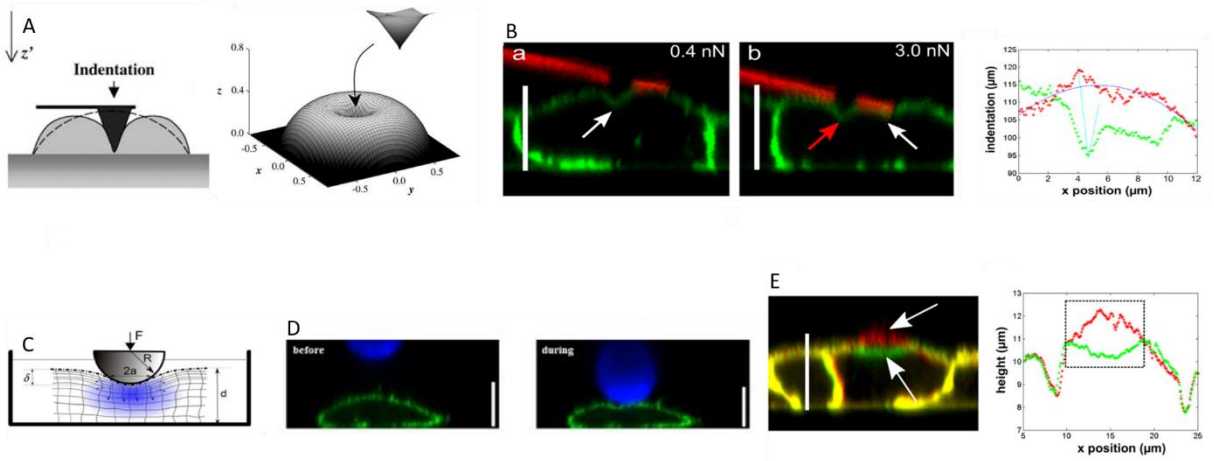

Figure 4 – Review from the literature showing the discrepancy between the theoretical indention geometry and the reality of indenting into a cell. (**A**) Theoretical indentations of a human red blood cell with a pyramidal tip by modelling (**left**) and 3-D representation (**right**) [From Sen, S., Subramanian, S. & Discher, D. E. Indentation and Adhesive Probing of a Cell Membrane with AFM: Theoretical Model and Experiments. Biophysical Journal 89, 3203–3213 (2005)]. (**B**) Indentations of a MDCK cell with a pyramidal tip visualized by confocal images (**left**) and indentation depth found during this indentation (**right**) [From Harris, A. & Charras, G. Experimental validation of atomic force microscopy-based cell elasticity measurements. Nanotechnology (2011)]. (**C**) Theoretical schematic indentation of a sample with a colloidal tip [From Esteki, M. H. *et al.* A new framework for characterization of poroelastic materials using indentation. Acta Biomater 102, 138–148 (2020)]. (**D**) Indentations of a HeLa cell with a colloidal tip visualized by confocal images before (**left**) and during (**right**) this indentation [From Moeendarbary, E. *et al.* The cytoplasm of living cells behaves as a poroelastic material. Nat Mater 12, 253–261 (2013)]. (**E**) Indentation of a MDCK cell with a colloidal tip visualized by confocal image (**left**) and indentation depth found during this indentation (**right**) [From Harris, A. & Charras, G. Experimental validation of atomic force microscopy-based cell elasticity measurements. Nanotechnology (2011)].

4. Conclusions

Our results and the literature, show that indentation geometry, in soft living cells, is not the same as the indenter geometry. Therefore, only relative Young's modulus comparisons made under the same conditions (same tip geometry, same fit length, same Poisson's ratio) are valid. However, to approach an absolute value of the Young's modulus, it is preferable to fit the approach curve on very small indentations. An alternative would be to check the actual geometry of the indentation with a side-view system for example and find new models or combinations of several models to account for that geometry (Harris, A. & Charras, G., 2011). Another solution would be to discard the geometry problem by providing a value independent from the indenter geometry. Actually, micro-rheology allows it, by calculating the loss tangent, which is the quotient of G'' (the loss modulus) and G' (the storage modulus). By dividing one by the other we get rid of the geometry issue (Rother et al., 2014).

From the confocal images of Fig. 4, it appears that the colloidal indenter is the best alternative to avoid the problems of indentation geometry. This literature review is based on 3 cell lines, and we have

carried out our work on one other cell line. It is therefore premature to generalize, but the question will have to be considered in the future. Future work on the mechanical properties of "very" soft cells will have to verify whether the shape of the indentor corresponds to the shape of the indentation, before applying a model for calculating Young's moduli that makes this assumption. Moreover, we have discussed here only the approach curves. Colloidal indenters could be problematic on retract curves due to too strong adhesions. It would then be problematic to take adhesion into account.

5. References

Abraham, S., Kaufman, Y., Perreault, F., Young, R., Bar-Zeev, E., 2021. Bursting out: linking changes in nanotopography and biomechanical properties of biofilm-forming Escherichia coli to the T4 lytic cycle. Npj Biofilms Microbiomes 7, 1–8. https://doi.org/10.1038/s41522-021-00195-7

Coceano, G., Yousafzai, M.S., Ma, W., Ndoye, F., Venturelli, L., Hussain, I., Bonin, S., Niemela, J., Scoles, G., Cojoc, D., Ferrari, E., 2015. Investigation into local cell mechanics by atomic force microscopy mapping and optical tweezer vertical indentation. Nanotechnology 27, 065102. https://doi.org/10.1088/0957-4484/27/6/065102

Deliorman, M., Janahi, F.K., Sukumar, P., Glia, A., Alnemari, R., Fadl, S., Chen, W., Qasaimeh, M.A., 2020. AFM-compatible microfluidic platform for affinity-based capture and nanomechanical characterization of circulating tumor cells. Microsyst. Nanoeng. 6, 20. https://doi.org/10.1038/s41378-020-0131-9

Dokukin, M.E., Guz, N.V., Sokolov, I., 2013. Quantitative Study of the Elastic Modulus of Loosely Attached Cells in AFM Indentation Experiments. Biophys. J. 104, 2123–2131. https://doi.org/10.1016/j.bpj.2013.04.019

Dramé, I., Formosa-Dague, C., Lafforgue, C., Chapot-Chartier, M.-P., Piard, J.-C., Castelain, M., Dague, E., 2020. Analysis of Homotypic Interactions of Lactococcus lactis Pili Using Single-Cell Force Spectroscopy. ACS Appl. Mater. Interfaces 12, 21411–21423. https://doi.org/10.1021/acsami.0c03069

Esteki, M.H., Alemrajabi, A.A., Hall, C.M., Sheridan, G.K., Azadi, M., Moeendarbary, E., 2020. A new framework for characterization of poroelastic materials using indentation. Acta Biomater. 102, 138–148. https://doi.org/10.1016/j.actbio.2019.11.010

Faria, E.C., Ma, N., Gazi, E., Gardner, P., Brown, M., Clarke, N.W., Snook, R.D., 2008. Measurement of elastic properties of prostate cancer cells using AFM. Analyst 133, 1498–1500. https://doi.org/10.1039/B803355B

Fischer, T., Hayn, A., Mierke, C.T., 2020. Effect of Nuclear Stiffness on Cell Mechanics and Migration of Human Breast Cancer Cells. Front. Cell Dev. Biol. 8.

Fredonnet, J., Foncy, J., Lamarre, S., Cau, J.-C., Trévisiol, E., Peyrade, J.-P., François, J.M., Séverac, C., 2013. Dynamic PDMS inking for DNA patterning by soft lithography. Microelectron. Eng. 111, 379–383.

Gibbs, E., Hsu, J., Barth, K., Goss, J.W., 2021. Characterization of the nanomechanical properties of the fission yeast (Schizosaccharomyces pombe) cell surface by atomic force microscopy. Yeast Chichester Engl. 38, 480–492. https://doi.org/10.1002/yea.3564

Harris, A. & Charras, G., 2011. Experimental validation of atomic force microscopy-based cell elasticity measurements. Nanotechnology.

Hiratsuka, S., Mizutani, Y., Toda, A., Fukushima, N., Kawahara, K., Tokumoto, H., Okajima, T., 2009. Power-Law Stress and Creep Relaxations of Single Cells Measured by Colloidal Probe Atomic Force Microscopy. Jpn. J. Appl. Phys. 48, 08JB17. https://doi.org/10.1143/JJAP.48.08JB17

Hurley, D.C., Turner, J.A., 2007. Measurement of Poisson's ratio with contact-resonance atomic force microscopy. J. Appl. Phys. 102, 033509. https://doi.org/10.1063/1.2767387

Hutter, J.L., Bechhoefer, J., 1993. Calibration of atomic-force microscope tips. Rev. Sci. Instrum. 64, 1868–1873. https://doi.org/10.1063/1.1143970
Jonas, O., Mierke, C.T., Käs, J.A., 2011. Invasive cancer cell lines exhibit biomechanical properties that are distinct from their noninvasive counterparts. Soft Matter 7, 11488–11495. https://doi.org/10.1039/C1SM05532A
Kontomaris, S.V., Stylianou, A., Malamou, A., 2022. Atomic Force Microscopy Nanoindentation Method on Collagen Fibrils. Materials 15, 2477. https://doi.org/10.3390/ma15072477
Kulkarni, S.G., Pérez-Domínguez, S., Radmacher, M., 2023. Influence of cantilever tip geometry and contact model on AFM elasticity measurement of cells. J. Mol. Recognit. 36, e3018. https://doi.org/10.1002/jmr.3018
Lagraulet, A., Foncy, J., Berteloite, B., Esteve, A., Blatche, M.-C., Malaquin, L., Vieu, C., 2015. InnoStamp 40™ and InnoScan 1100AL™: a complete automated platform for microstructured cell arrays. Nat. Methods 12, i–iii. https://doi.org/10.1038/nmeth.f.383
Lee, H., Bonin, K., Guthold, M., 2021. Human mammary epithelial cells in a mature, stratified epithelial layer flatten and stiffen compared to single and confluent cells. Biochim. Biophys. Acta Gen. Subj. 1865, 129891. https://doi.org/10.1016/j.bbagen.2021.129891
Lee, J.-J., Rao, S., Kaushik, G., Azeloglu, E.U., Costa, K.D., 2018. Dehomogenized Elastic Properties of Heterogeneous Layered Materials in AFM Indentation Experiments. Biophys. J. 114, 2717–2731. https://doi.org/10.1016/j.bpj.2018.04.036
Lekka, M., Laidler, P., Gil, D., Lekki, J., Stachura, Z., Hrynkiewicz, A.Z., 1999. Elasticity of normal and cancerous human bladder cells studied by scanning force microscopy. Eur. Biophys. J. 28, 312–316. https://doi.org/10.1007/s002490050213
Lekka, M., Pogoda, K., Gostek, J., Klymenko, O., Prauzner-Bechcicki, S., Wiltowska-Zuber, J., Jaczewska, J., Lekki, J., Stachura, Z., 2012. Cancer cell recognition – Mechanical phenotype. Micron, Special issue on AFM in Biology & Bionanomedicine 43, 1259–1266. https://doi.org/10.1016/j.micron.2012.01.019
Lin, D.C., Dimitriadis, E.K., Horkay, F., 2007. Robust Strategies for Automated AFM Force Curve Analysis—I. Non-adhesive Indentation of Soft, Inhomogeneous Materials. J. Biomech. Eng. 129, 430–440. https://doi.org/10.1115/1.2720924
Moeendarbary, E., Valon, L., Fritzsche, M., Harris, A.R., Moulding, D.A., Thrasher, A.J., Stride, E., Mahadevan, L., Charras, G.T., 2013. The cytoplasm of living cells behaves as a poroelastic material. Nat. Mater. 12, 253–261. https://doi.org/10.1038/nmat3517
Nikkhah, M., Strobl, J.S., Schmelz, E.M., Agah, M., 2011. Evaluation of the influence of growth medium composition on cell elasticity. J. Biomech. 44, 762–766. https://doi.org/10.1016/j.jbiomech.2010.11.002
Omidvar, R., Tafazzoli-shadpour, M., Shokrgozar, M.A., Rostami, M., 2014. Atomic force microscope-based single cell force spectroscopy of breast cancer cell lines: An approach for evaluating cellular invasion. J. Biomech. 47, 3373–3379. https://doi.org/10.1016/j.jbiomech.2014.08.002
Orzechowska, B., Awsiuk, K., Wnuk, D., Pabijan, J., Stachura, T., Soja, J., Sładek, K., Raczkowska, J., 2022. Discrimination between NSIP- and IPF-Derived Fibroblasts Based on Multi-Parameter Characterization of Their Growth, Morphology and Physic-Chemical Properties. Int. J. Mol. Sci. 23, 2162. https://doi.org/10.3390/ijms23042162
Parihar, K., Nukpezah, J., Iwamoto, D.V., Janmey, P.A., Radhakrishnan, R., 2022. Data driven and biophysical insights into the regulation of trafficking vesicles by extracellular matrix stiffness. iScience 25, 104721. https://doi.org/10.1016/j.isci.2022.104721
Park, S., Koch, D., Cardenas, R., Käs, J., Shih, C.K., 2005. Cell Motility and Local Viscoelasticity of Fibroblasts. Biophys. J. 89, 4330–4342. https://doi.org/10.1529/biophysj.104.053462
Pogoda, K., Jaczewska, J., Wiltowska-Zuber, J., Klymenko, O., Zuber, K., Fornal, M., Lekka, M., 2012. Depth-sensing analysis of cytoskeleton organization based on AFM data. Eur. Biophys. J. 41, 79–87. https://doi.org/10.1007/s00249-011-0761-9

Radmacher, M., Fritz, M., Kacher, C.M., Cleveland, J.P., Hansma, P.K., 1996. Measuring the viscoelastic properties of human platelets with the atomic force microscope. Biophys. J. 70, 556–567.

Ramos, J.R., Pabijan, J., Garcia, R., Lekka, M., 2014. The softening of human bladder cancer cells happens at an early stage of the malignancy process. Beilstein J. Nanotechnol. 5, 447–457. https://doi.org/10.3762/bjnano.5.52

Rico, F., Roca-Cusachs, P., Gavara, N., Farré, R., Rotger, M., Navajas, D., 2005. Probing mechanical properties of living cells by atomic force microscopy with blunted pyramidal cantilever tips. Phys. Rev. E 72, 021914. https://doi.org/10.1103/PhysRevE.72.021914

Roduit, C., Saha, B., Alonso-Sarduy, L., Volterra, A., Dietler, G., Kasas, S., 2012. OpenFovea: open-source AFM data processing software. Nat. Methods 9, 774–775. https://doi.org/10.1038/nmeth.2112

Roduit, C., Sekatski, S., Dietler, G., Catsicas, S., Lafont, F., Kasas, S., 2009. Stiffness Tomography by Atomic Force Microscopy. Biophys. J. 97, 674–677. https://doi.org/10.1016/j.bpj.2009.05.010

Rother, J., Nöding, H., Mey, I., Janshoff, A., 2014. Atomic force microscopy-based microrheology reveals significant differences in the viscoelastic response between malign and benign cell lines. Open Biol. 4, 140046. https://doi.org/10.1098/rsob.140046

Sader, J.E., Chon, J.W.M., Mulvaney, P., 1999. Calibration of rectangular atomic force microscope cantilevers. Rev. Sci. Instrum. 70, 3967–3969. https://doi.org/10.1063/1.1150021

Schillers, H., Rianna, C., Schäpe, J., Luque, T., Doschke, H., Wälte, M., Uriarte, J.J., Campillo, N., Michanetzis, G.P.A., Bobrowska, J., Dumitru, A., Herruzo, E.T., Bovio, S., Parot, P., Galluzzi, M., Podestà, A., Puricelli, L., Scheuring, S., Missirlis, Y., Garcia, R., Odorico, M., Teulon, J.-M., Lafont, F., Lekka, M., Rico, F., Rigato, A., Pellequer, J.-L., Oberleithner, H., Navajas, D., Radmacher, M., 2017. Standardized Nanomechanical Atomic Force Microscopy Procedure (SNAP) for Measuring Soft and Biological Samples. Sci. Rep. 7, 5117. https://doi.org/10.1038/s41598-017-05383-0

Sen, S., Subramanian, S., Discher, D.E., 2005. Indentation and Adhesive Probing of a Cell Membrane with AFM: Theoretical Model and Experiments. Biophys. J. 89, 3203–3213. https://doi.org/10.1529/biophysj.105.063826

Sharma, S., Santiskulvong, C., Bentolila, L.A., Rao, J., Dorigo, O., Gimzewski, J.K., 2012. Correlative nanomechanical profiling with super-resolution F-actin imaging reveals novel insights into mechanisms of cisplatin resistance in ovarian cancer cells. Nanomedicine Nanotechnol. Biol. Med. 8, 757–766. https://doi.org/10.1016/j.nano.2011.09.015

Sirghi, L., Ponti, J., Broggi, F., Rossi, F., 2008. Probing elasticity and adhesion of live cells by atomic force microscopy indentation. Eur. Biophys. J. 37, 935–945. https://doi.org/10.1007/s00249-008-0311-2

Song, J., Meng, X., Zhang, H., Sun, L., Xie, H., 2018. In Situ Quantification the Complex Poisson's Ratio of Single Cells Using a Magnetic-Drive Dynamic Atomic Force Microscopy Approach. IEEE Trans. Nanotechnol. 17, 680–683. https://doi.org/10.1109/TNANO.2018.2799212

Staunton, J.R., Doss, B.L., Lindsay, S., Ros, R., 2016. Correlating confocal microscopy and atomic force indentation reveals metastatic cancer cells stiffen during invasion into collagen I matrices. Sci. Rep. 6, 19686. https://doi.org/10.1038/srep19686

Strobl, J.S., Nikkhah, M., Agah, M., 2010. Actions of the anti-cancer drug suberoylanilide hydroxamic acid (SAHA) on human breast cancer cytoarchitecture in silicon microstructures. Biomaterials 31, 7043–7050. https://doi.org/10.1016/j.biomaterials.2010.05.023

te Riet, J., Katan, A.J., Rankl, C., Stahl, S.W., van Buul, A.M., Phang, I.Y., Gomez-Casado, A., Schön, P., Gerritsen, J.W., Cambi, A., Rowan, A.E., Vancso, G.J., Jonkheijm, P., Huskens, J., Oosterkamp, T.H., Gaub, H., Hinterdorfer, P., Figdor, C.G., Speller, S., 2011. Interlaboratory round robin on cantilever calibration for AFM force spectroscopy. Ultramicroscopy 111, 1659–1669. https://doi.org/10.1016/j.ultramic.2011.09.012

Wu, P.-H., Aroush, D.R.-B., Asnacios, A., Chen, W.-C., Dokukin, M.E., Doss, B.L., Durand-Smet, P., Ekpenyong, A., Guck, J., Guz, N.V., Janmey, P.A., Lee, J.S.H., Moore, N.M., Ott, A., Poh, Y.-C.,

Ros, R., Sander, M., Sokolov, I., Staunton, J.R., Wang, N., Whyte, G., Wirtz, D., 2018. A comparison of methods to assess cell mechanical properties. Nat. Methods 15, 491–498. https://doi.org/10.1038/s41592-018-0015-1

Xu, W., Mezencev, R., Kim, B., Wang, L., McDonald, J., Sulchek, T., 2012. Cell stiffness is a biomarker of the metastatic potential of ovarian cancer cells. PloS One 7, e46609. https://doi.org/10.1371/journal.pone.0046609

Zemła, J., Bobrowska, J., Kubiak, A., Zieliński, T., Pabijan, J., Pogoda, K., Bobrowski, P., Lekka, M., 2020. Indenting soft samples (hydrogels and cells) with cantilevers possessing various shapes of probing tip. Eur. Biophys. J. 49, 485–495. https://doi.org/10.1007/s00249-020-01456-7

Acknowledgements

We deeply thank C. Blatché and S. Assie-Souleille and the carac platform of LAAS-CNRS for the cell culture room support. The work was partly supported by the French Renatech network. And, in particular, we thank V. Fabre for helping us with SEM images. We also thank the BIOSOFT joint laboratory for the microcontact-printing part. This work was supported by grants from the Agence Nationale de la Recherche (ANR) AutoBioTip - ANR-20-CE42-0017. This work, bearing the reference EUR CARe N°ANR-18-EURE-0003, benefited from a government grant managed by the Agence Nationale de la Recherche under the Programme Investissements d'Avenir. ED is a researcher at Centre National de la Recherche Scientifique (CNRS).